Electronic Supplementary Information for

Green synthesis of redox-active riboflavin integrated Ni-MOF and its versatile electrocatalytic applications towards oxygen evolution and reduction, and HMF oxidation reactions

Pandiaraj Sekar,[a] Punitharaj Vasanthakumar,[a] Ramasamy Shanmugam,[b] Shanmugam Senthil Kumar,[c] Stefano Agnoli,[d] Rajasekharan Jayakumari Deepak,[a] Murugan Karthik,[a] Nattamai Bhuvanesh,[e] and Ramasamy Karvembu*,[a]

[a]*Department of Chemistry, National Institute of Technology, Tiruchirappalli 620015, India, E-mail address: kar@nitt.edu (R. Karvembu); Fax: +91 431 2500133; Tel: +91 431 2503636*

[b]*CO_2 Research and Green Technologies Center, Vellore Institute of Technology (VIT), Vellore-632014, India*

[c]*Electrodics and Electrocatalysis Division, CSIR-Central Electrochemical Research Institute, Karaikudi 630006, India*

[d]*Department of Chemical Sciences, and Consorzio Interuniversitario Reattività Chimica e Catalisi-CIRCC, University of Padova, Via F. Marzolo 1 35131 Padova, Italy*

[e]*Department of Chemistry, Texas A & M University, College Station, Texas 77842, United States*

Physical methods

PANalytical X'Pert Pro machine equipped with Cu Kα (1.5418 Å) source was employed for the powder X-ray diffraction (PXRD) analyses of the prepared MOFs. The analyses were carried out in the 2θ range of 0-60° with the sweep rate of 0.5° per min. The morphology was analyzed using a TECNAI G2 F30 high-resolution transmission electron microscope (HR-TEM) at an operating potential of 300 kV. The samples for TEM analyses were obtained by adding the materials in isopropyl alcohol (IPA) followed by dropping the dispersion onto a copper grid and drying under *vacuum* oven for 12 h. Scanning electron microscope (SEM) imaging were performed using Quanta 200 3D microscope furnished with an EDX (Energy dispersive X-ray) attachment (Operating voltage = 30 kV). X-ray photoelectron spectra (XPS) were measured using a VG Microtech Multilab ESCA 3000 spectrometer equipped with a Mg Kα X-ray source (hν = 1253.6 eV). Nitrogen adsorption-desorption measurements were carried out at 77 K by employing a Quantachrome Quadrasorb automatic volumetric machine. Prior to the gas adsorption measurements, the samples were pre-activated at room temperature for 24 h and at 100 °C for 36 h under ultrahigh vacuum (10-8 mbar).

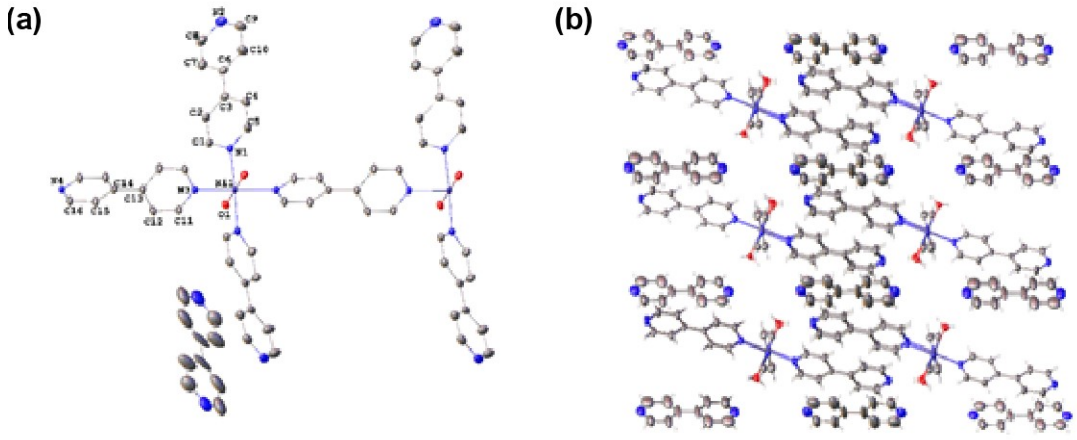

Fig. S1. (a and b) Crystal structures of pristine Ni-MOF.

Data collection

A Leica MZ 75 microscope was used to identify a suitable blue block with very well-defined faces with dimensions (max, intermediate and min) 0.365 × 0.268 × 0.218 mm^3 from a representative sample of crystals of the same habit. The crystal mounted on a nylon loop was then placed in a cold nitrogen stream maintained at 110 K. A Bruker Quest X-ray (fixed-Chi geometry) diffractometer was employed for crystal screening, unit cell determination and data collection. The goniometer was controlled using the APEX3 software suite.[1] The sample was optically centered with the aid of a video camera such that no translations were observed as the crystal was rotated through all positions. The X-ray radiation employed was generated from a Mo-Iμs X-ray tube (K_α = 0.71073Å). 45 data frames were taken at widths of 1°. These reflections were used to determine the unit cell. The unit cell was verified by examination of the *h k l* overlays on several frames of data. No super-cell or erroneous reflections were observed. After careful examination of the unit cell, an extended data collection procedure (5 sets) was initiated using omega scans.

Data reduction, structure solution and refinement

Integrated intensity information for each reflection was obtained by reduction of the data frames with the program APEX3.[1] The integration method employed a three-dimensional profiling algorithm, and all data were corrected for Lorentz and polarization factors, as well as for crystal decay effects. Finally, the data were merged and scaled to produce a suitable data set. The absorption correction program SADABS was employed to correct the data for absorption effects.[2] Systematic reflection conditions and statistical tests of the data suggested the space group *C*2/*c*. A solution was obtained readily (*Z* = 4; *Z*' = 0.5) using XT/XS in APEX3.[1,3] Hydrogen

atoms were placed in idealized positions and were set riding on the respective parent atoms. All non-hydrogen atoms were refined with anisotropic thermal parameters. Residual electron density peaks around $C_{10}H_8N_2$ molecule indicated disorder of this molecule. Also, additional residual electron density peaks which could not be successfully modelled were present. These were masked using Olex2. The procedure indicates 82 electrons per asymmetric molecule, which correspond closely to a molecule of $C_{10}H_8N_2$. Absence of additional symmetry was confirmed using PLATON (ADDSYM). The structure was refined (weighted least squares refinement on F^2) to convergence.[3,4] Olex2 was employed for the final data presentation and structure plots.[4]

Table 1. Crystal data and structure refinement for Ni-MOF

Empirical formula	$C_{38.84}H_{35.07}N_{7.77}NiO_2$	
Formula weight	701.35	
Temperature	110.0 K	
Wavelength	0.71073 Å	
Crystal system	Monoclinic	
Space group	*C 1 2/c 1*	
Unit cell dimensions	a = 17.4793(18) Å	□ = 90°
	b = 11.3654(18) Å	□□= 93.506(2)°
	c = 24.468(3) Å	□ = 90°
Volume	4851.6(11) $Å^3$	
Z	4	
Density (calculated)	0.960 Mg/m^3	
Absorption coefficient	0.433 mm^{-1}	
F(000)	1466	
Crystal size	0.365 × 0.268 × 0.218 mm^3	
Theta range for data collection	2.139 to 27.544°.	
Index ranges	-22<=h<=22, -14<=k<=14, -31<=l<=31	
Reflections collected	45498	
Independent reflections	5575 [R(int) = 0.0414]	
Completeness to theta = 25.242°	99.5%	
Absorption correction	Semi-empirical from equivalents	
Max. and min. transmission	0.4305 and 0.3890	
Refinement method	Full-matrix least-squares on F^2	
Data / restraints / parameters	5575 / 72 / 235	
Goodness-of-fit on F^2	1.088	
Final R indices [I>2sigma(I)]	R1 = 0.0643, wR2 = 0.1789	
R indices (all data)	R1 = 0.0703, wR2 = 0.1835	
Largest diff. peak and hole	1.018 and -0.545 e.$Å^{-3}$	

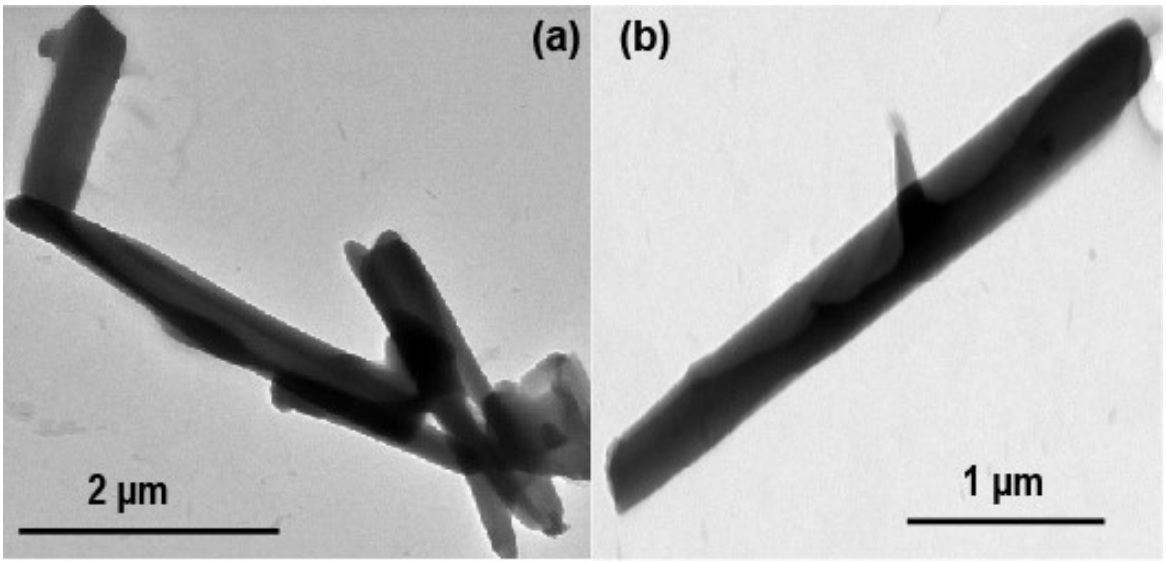

Fig. S2. (a and b) TEM images of Ni-MOF at different magnifications.

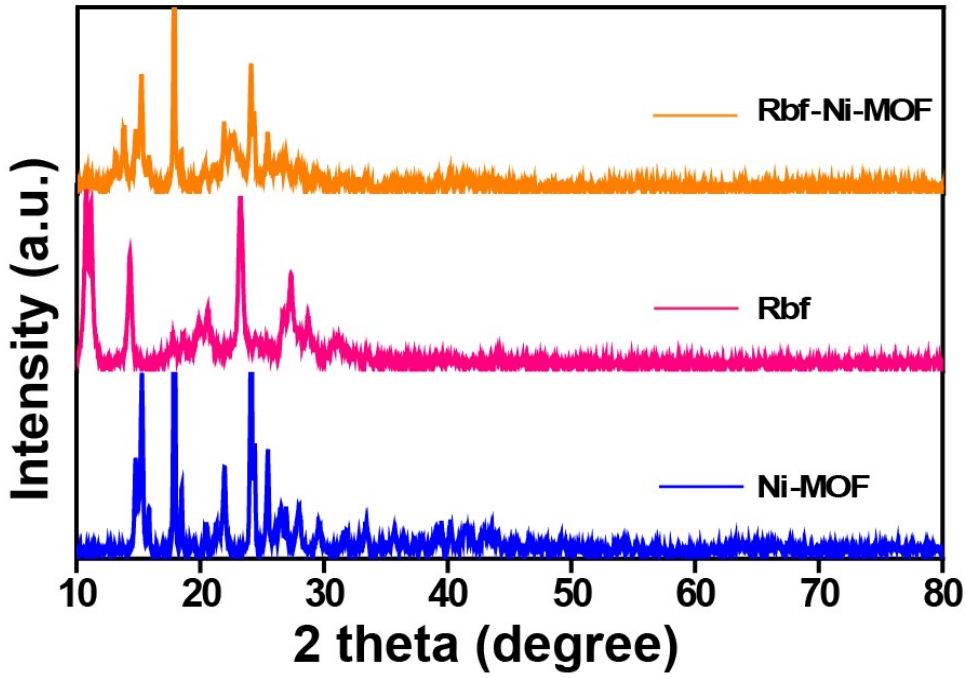

Fig. S3. PXRD patterns of pristine Ni-MOF, Rbf and Rbf- Ni-MOF.

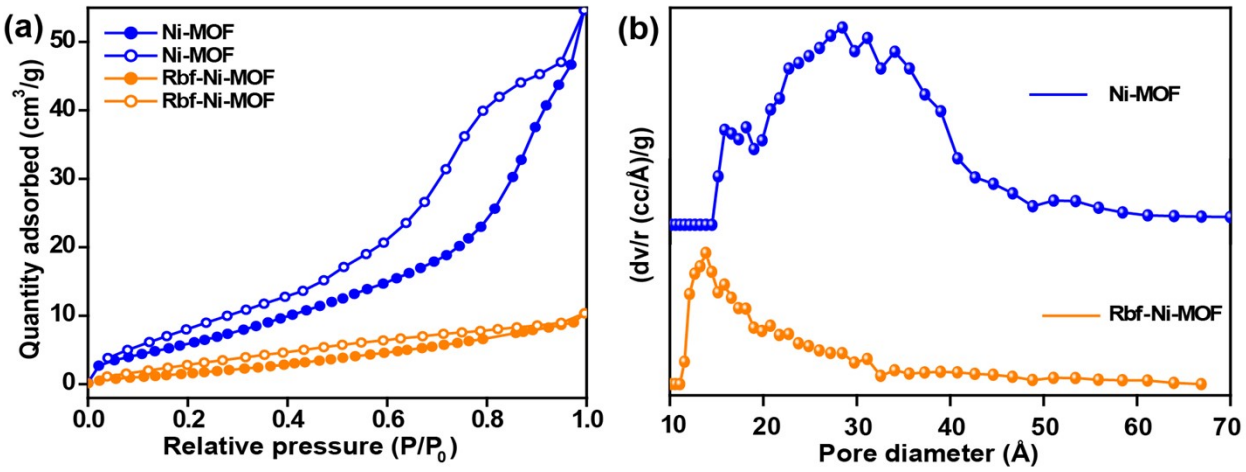

Fig. S4. (a) N_2 adsorption analyses and (b) Pore size distribution analyses of Ni-MOF and Rbf-Ni-MOF.

Thermal stability analysis

To understand the thermal stability and interaction between Ni-MOF and Rbf, Rbf-Ni-MOF was heated at 140 °C for 24 h. If there are weak interactions such as van der Waals, we should get back the original blue colour. Interestingly, the color of Rbf-Ni-MOF remains greenish yellow even after heating; it means that the material is quite stable. Hence, there may be covalent interactions exist between Ni-MOF and Rbf .

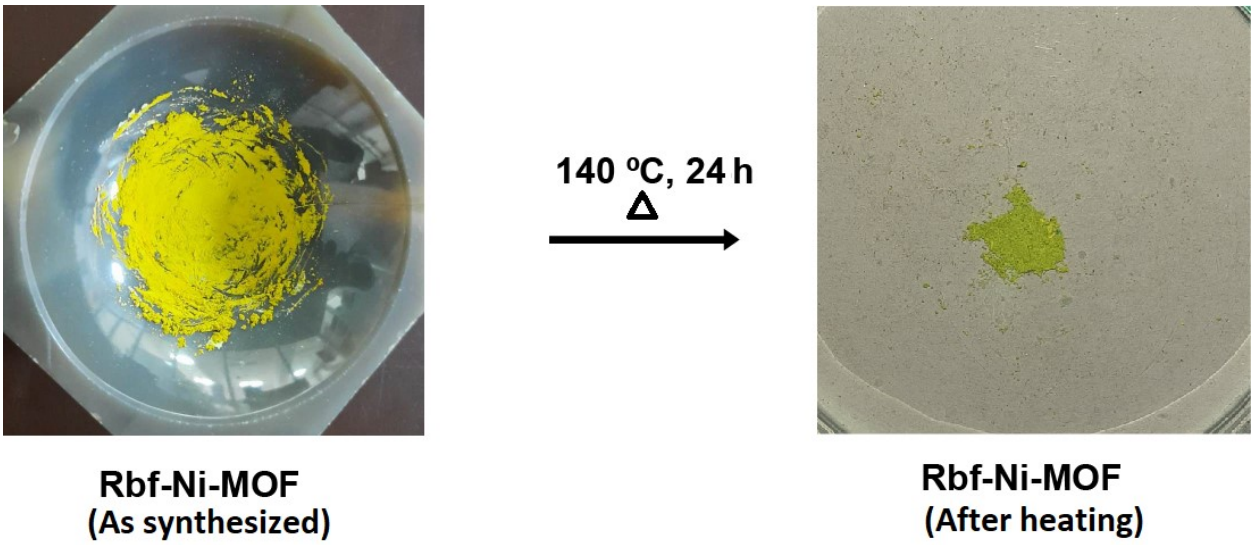

Fig. S5. Digital images of as synthesized and heated Rbf-Ni-MOF.

Electrical conductivity measurements by four-probe method

Initially, a pellet of Rbf-Ni-MOF (Thickness = 0.65 mm) was prepared. Conductivity experiment was carried out by keeping the pellet on a non-conducting surface, and the experiment was performed by the four-probe technique utilizing a Keysight B-2901A source measure unit with a Kelvin four-probe. The following equations were used for calculating the conductivity of the sample.

$$K = \frac{1}{\rho}$$

$$\rho = \frac{2\pi S \frac{V}{I}}{G_7(\frac{W}{S})}$$

where K = conductivity (S cm^{-1}), ρ = resistivity (Ω cm), $G_7(\frac{W}{S})$ = correction factor, W = thickness of the pellet, S = probe spacing (2 mm), V = voltage (V) and I = current (A).

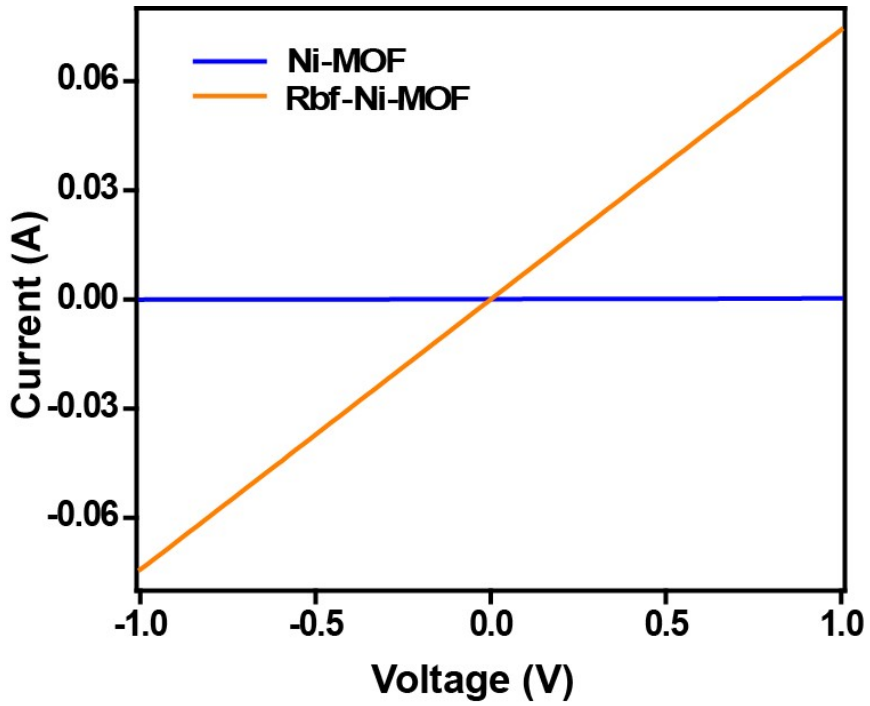

Fig. S6. I-V curves of Ni-MOF, Rbf and Rbf-Ni-MOF.

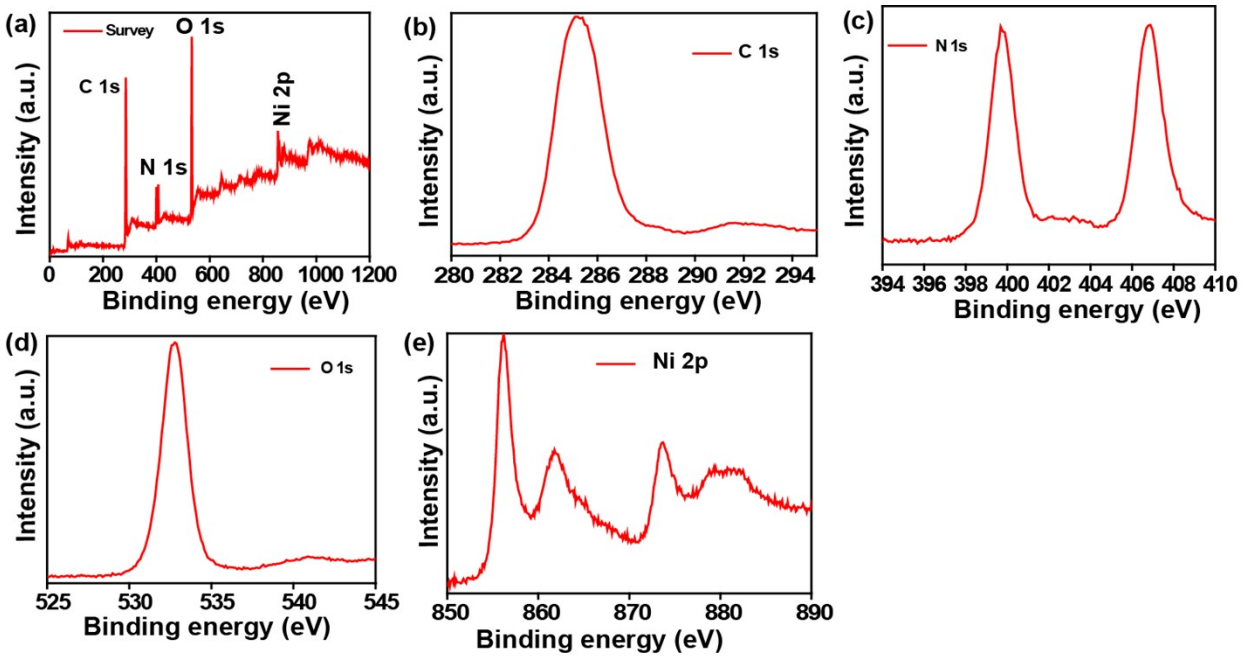

Fig. S7. (a) Survey, (b) C 1s, (c) N 1s, (d) O 1s and (e) Ni 2p XPS spectra of Rbf-Ni-MOF.

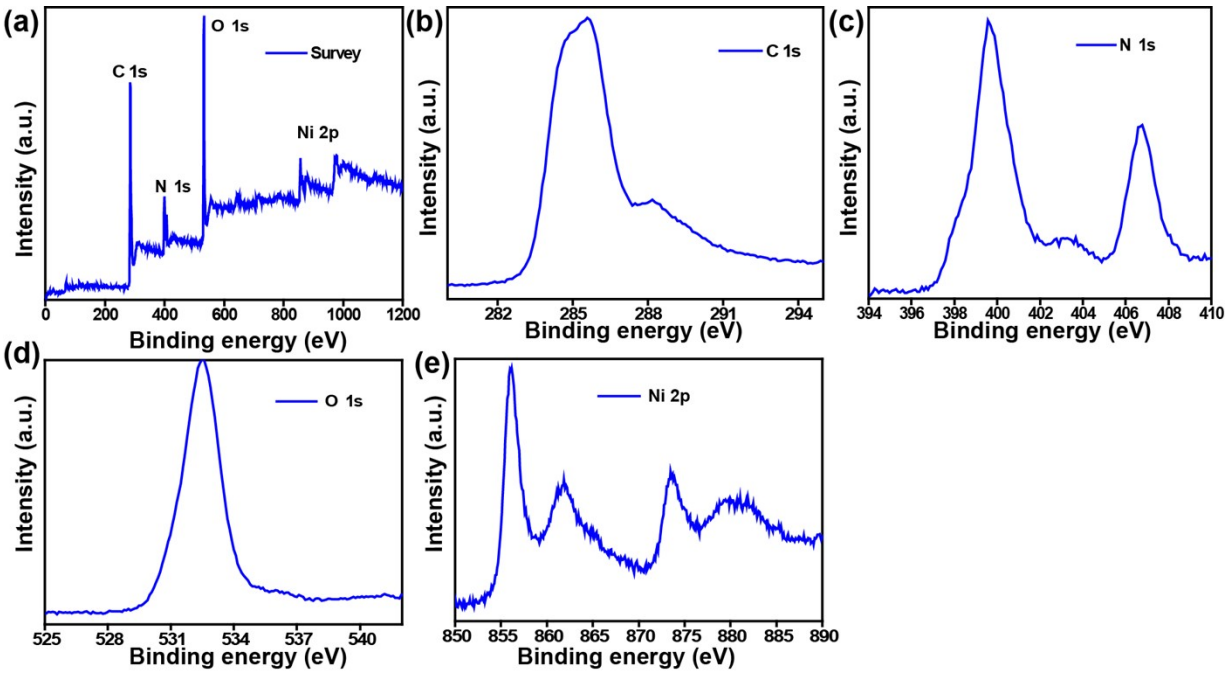

Fig. S8. (a) Survey, (b) C 1s, (c) N 1s, (d) O 1s and (e) Ni 2p XPS spectra of Ni-MOF.

Table S1. Summary of the elemental composition of the prepared samples.

Sample	C (wt. %)	N (wt. %)	O (wt. %)	Ni (wt. %)
Ni-MOF	**64.78**	**5.9**	**24.1**	**5.0**
Rbf-Ni-MOF	**65.4**	**7.5**	**22.1**	**4.65**

Electrochemical studies of the prepared catalysts

Autolab PGSTAT 30 (Ecochemie) instrument was used to perform the entire electrochemical analyses in a standard three-electrode cell. The Ohmic drop value of OER experiments was compensated to deal with the standing voltage drop between the working electrode and reference electrode by Ivium software. Ag/AgCl (in saturated KCl) and graphite rod were employed as reference and counter electrodes, respectively. Glassy carbon (GC) (3 mm

diameter) embedded in Teflon was used as a working electrode. Prior to the analyses, the GC electrode was cleaned on a polishing cloth using 0.3 µm alumina slurry followed by washing many times with ethanol and water. Thin film of the sample was coated on the working electrode as follows: Known quantity (5 mg) of the catalyst was added to 1 mL of ethanol-water (3:2) mixture with ultra-sonication. 5 µL aliquot of the ink was directly placed on the GC electrode with the help of a micro syringe. Subsequently, 3 µL of 0.1% Nafion® solution in ethanol was drop casted on the surface as a binder. This electrode was allowed to dry in air for 3 h and instantly applied as working electrode. Alkaline (0.1 M KOH) solution was employed as an electrolyte throughout the electrochemical analyses. Rotating ring disc electrode (RRDE) studies were performed on a Pine instrument keeping Pt ring working electrode. All the cyclic and linear sweep voltammetry and RRDE experiments were conducted at a scan rate of 10 mV/s. During the RDE experiments, to create oxygen saturated and oxygen-free environments, O_2 and N_2 gases were purged in the electrolyte solution, respectively. The number of electrons transferred per oxygen molecule during the oxygen reduction reaction was calculated by applying Koutecky–Levich (K-L) equation, and the yield of H_2O_2 was calculated using RRDE experiments. The K-L equation relates the inverse of the current density (j^{-1}) and inverse of the square root of the rotation speed ($\omega^{-0.5}$), and can be written as follows

$$\frac{1}{j_{lim}} = \frac{1}{j_k} + \frac{1}{B\,\omega^{0.5}}$$

$$B = 0.62nF\,(D_o)^{2/3}v^{-1/6}C_{O2}$$

where, j_k is the kinetic current density, ω is the angular velocity and B is associated to the diffusion limiting current density and stated in the form of equation. In the equation, F is the Faraday constant (F = 96485 C mol^{-1}), n is the number of electrons involved, C_{O2} is the bulk

concentration of O_2 (1.2×10^{-3} mol l^{-1}), v is the kinematic viscosity of the electrolyte (v = 0.1 m^2 s^{-1}) and D_o is the diffusion coefficient of O_2 in 0.1 M KOH (1.9×10^{-5} cm^2 s^{-1}). K-L plots, which relates the limiting current density (j_{lim}) and square root of rotation speed ($\omega^{0.5}$), are mentioned. It shows a linear relation between the current density and square root of the rotation speed in the potential range of -0.25 to -0.6 V. The yields of H_2O_2 formed during RRDE analyses were determined from the following formula

$$\% \text{ of } H_2O_2 = \{(200 * \frac{I_r}{N} / (I_d + \frac{I_r}{N})\}$$

where I_r = ring current, I_d = disc current and N = collection efficiency.

ECSA analysis

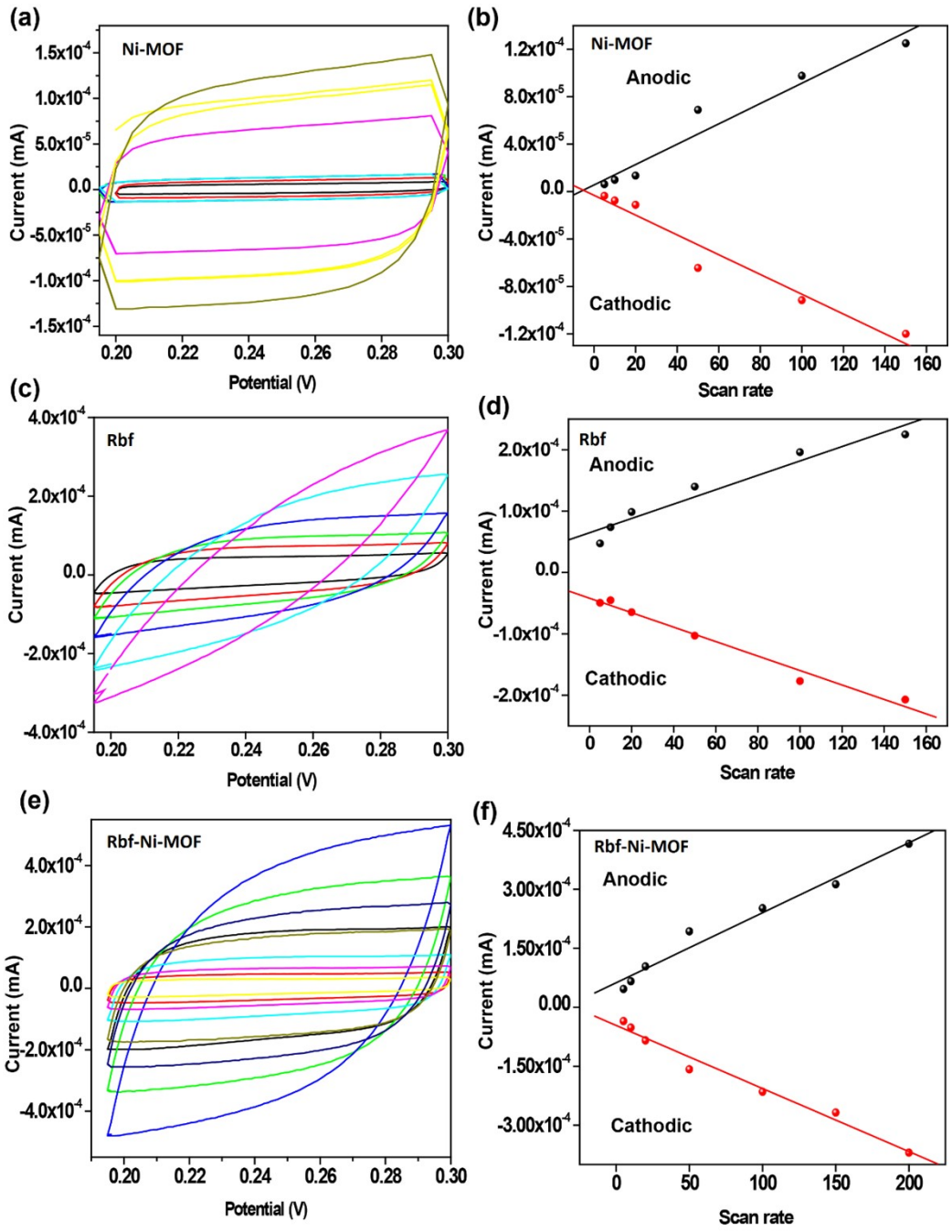

Fig. S9. CV profiles (a,c,e,) in the double layer capacitance region at various sweep rate and resultant current-sweep rate plots (b,d,f,) for Ni-MOF (a,b), Rbf (c,d) and Rbf-Ni-MOF (e,f).

Post XPS analyses of Rbf-Ni-MOF

After the electrolysis, the electrodes were excluded carefully from the cell. The spent catalysts were isolated by scratching from the surface of the electrodes and transferred to deionized water. After washing many times with deionized water followed by drying under vacuum, the resulting powdered materials were directly used for XPS measurements. The same protocol was followed for the post analysis of spent catalysts in HMF Oxidation reactions.

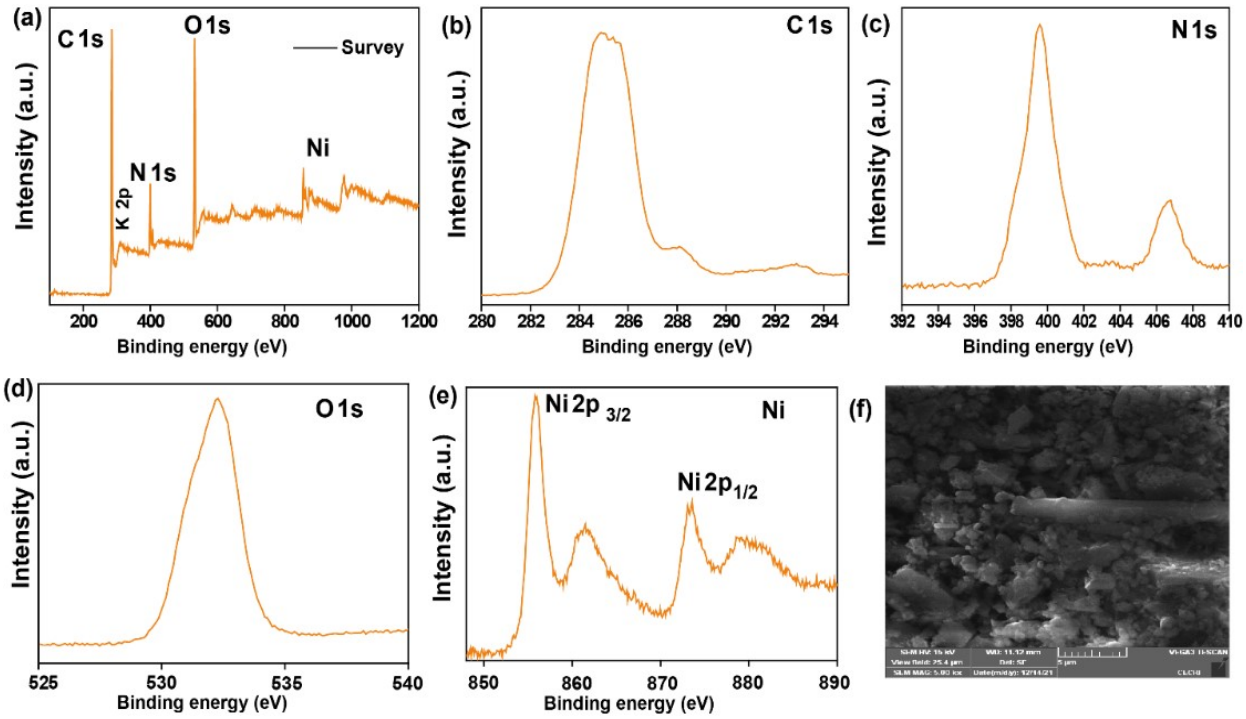

Fig. S10. (a) Survey, (b) C 1s, (c) N 1s, (d) O 1s and (e) Ni 2p XPS spectra of the used Rbf- Ni-MOF.

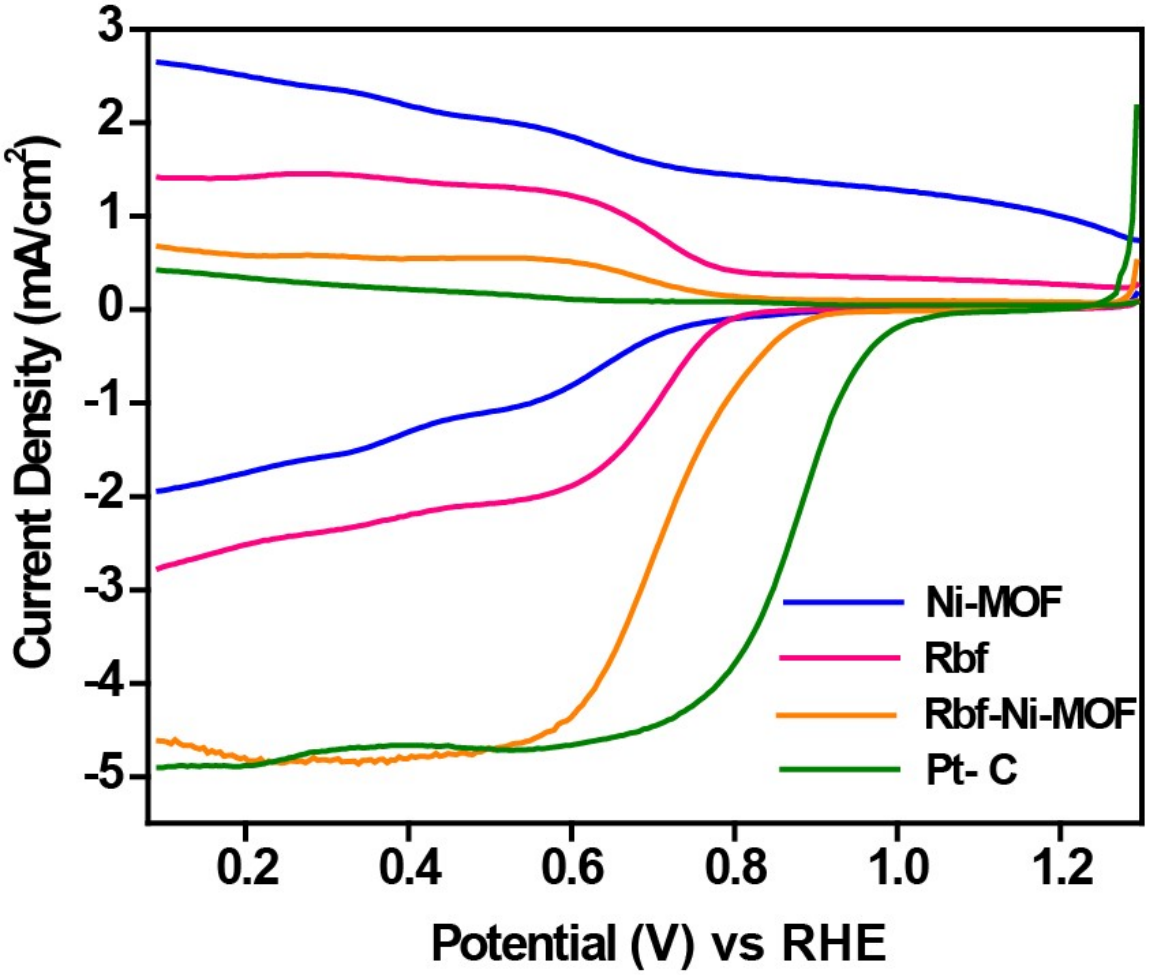

Fig. S11. Analyses of electrocatalytic ORR in 0.1 M KOH. LSVs are measured at a rotating speed of 1600 rpm of the working electrode and scan rate 0.01 V s^{-1}.

Electrocatalytic oxidation of HMF

HMF oxidation was performed in a H-type electrochemical cell in which both the anode and cathode chambers were separated by Nafion (117) membrane. Rbf-Ni-MOF coated Ni foam (with a loading of 1 mg/cm^2) was used as a working electrode, Ag/AgCl (saturated with KCl) as a reference electrode and Pt wire as a counter electrode in 1 M KOH electrolyte. Equal volume (50 mL) of electrolyte (1 M KOH) was introduced into both the anode and cathode chambers. Further, known quantity of HMF (10 mmol) was directly added into the anodic chamber to trigger the HMF oxidation. Pt wire was placed in the cathodic chamber. At a scan rate of 10 mV/s, the potential range was scanned cyclically.

Quantification of FDCA by HPLC analyses

For the effective quantification of reactant and product during the oxidation of HMF, aliquots (1 mL) of the electrolyte solution were collected at different time intervals. The collected aliquots were diluted, neutralized (pH = 7) and analysed through high-performance liquid chromatography (HPLC, Shimadzu Prominence LC-20A) using UV-Vis detector with the detection wavelength of 265 nm. Shimadzu C 18 column with the dimensions of 4.6 mm × 150 mm × 5 µm was employed for the HPLC analysis. A mixed mobile phase [Ammonium formate (5 mM, 70 vol %) and methanol (30 vol %)] was used at the flow rate of 1.0 mL/min. The quantification of the product was achieved using calibration curves obtained from the known concentrations of standard HMF and FDCA. Standard FDCA solutions of various concentrations (5, 4, 3, 2 and 1 mg/L) were used to derive calibration curve.

Structural models and computational calculations

Quantum Espresso was used to perform all the computational calculations. Electrons were dealt utilizing the generalized gradient approximation (GGA) with the Perdew–Burke–Ernzerhof (PBE) exchange-correlation functional in first principle calculations. The GGA-PBE and GGA-PBE+U levels were used to find structural energy minimization and electronic characteristics, respectively. The wavefunction had a kinetic energy cut off at 60 Ry with the charge of 480 Ry. To integrate the Brillouin zone, a gamma k-point mesh was used.

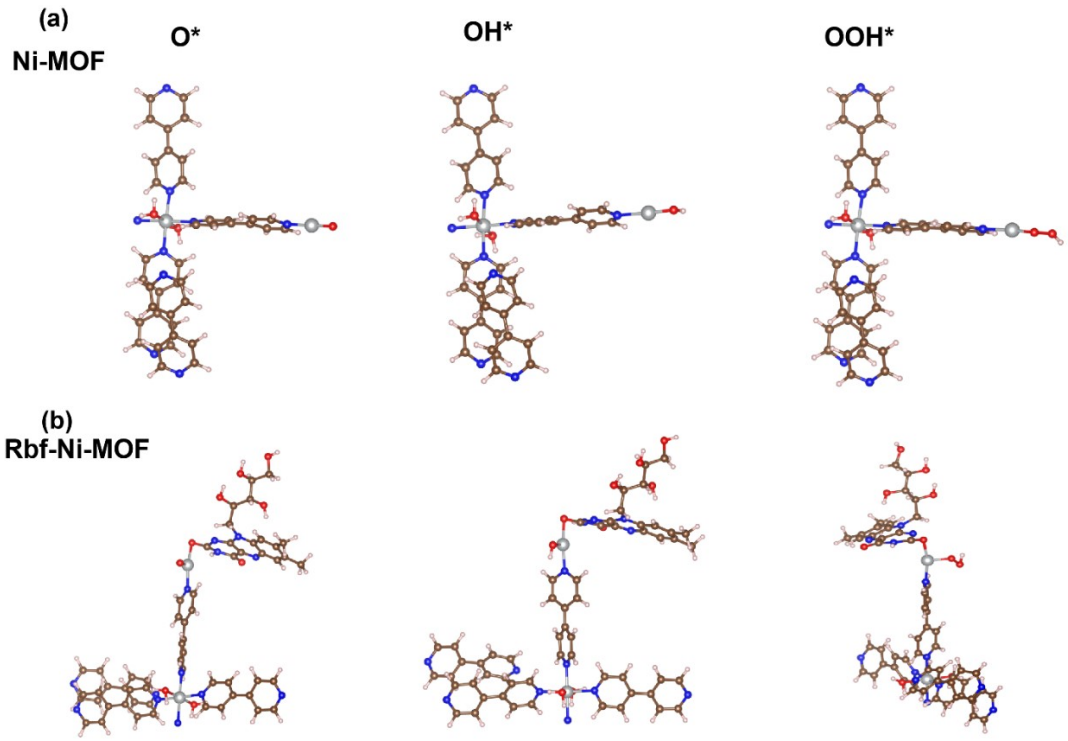

Fig. S12. (a) and (b) On the Ni-MOF and Rbf-Ni-MOF, energy minimized structures of the different intermediates involved in OER and ORR. The Ni, O, N, C and H atoms are represented by the grey, red, blue, brown and pink colours, respectively.

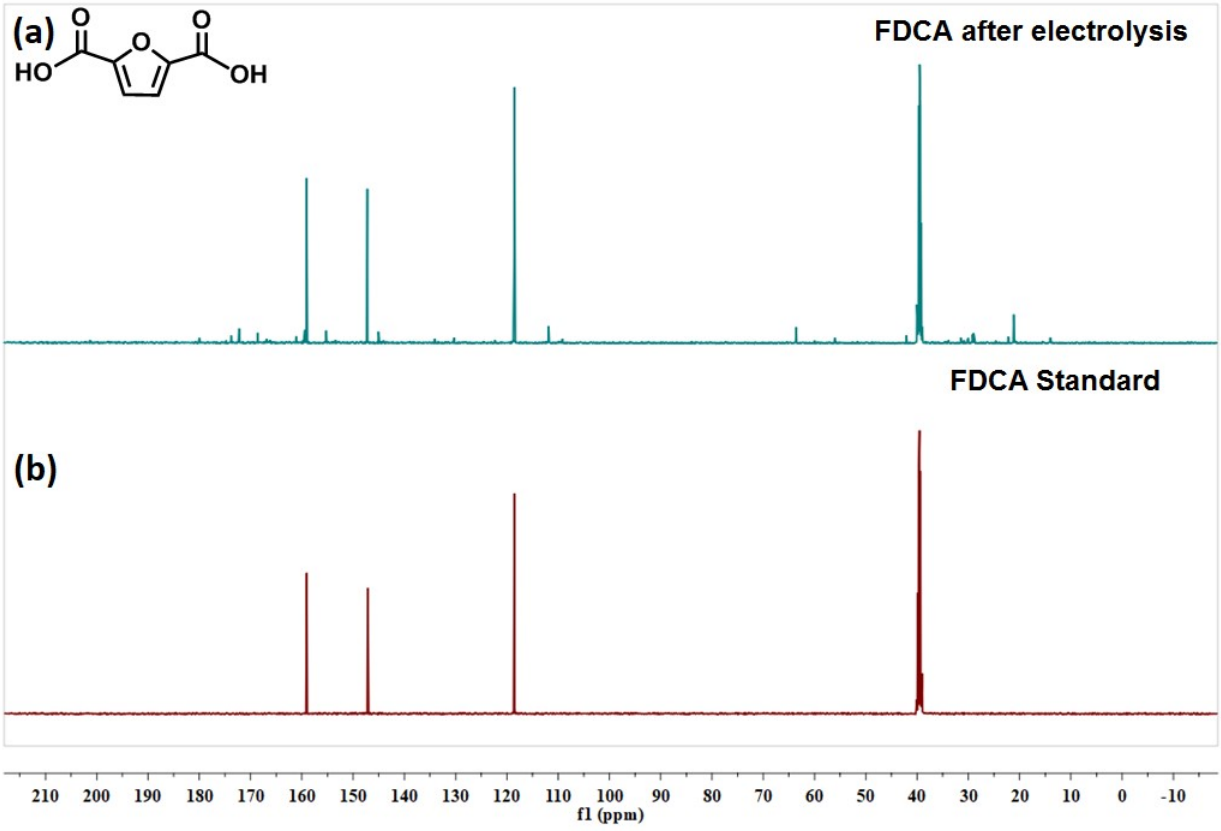

Fig. S13. ^{13}C-NMR spectra (DMSO-d_6) of (a) standard FDCA, (b) electrolyte collected from the anodic chamber after electrolysis (2 h).

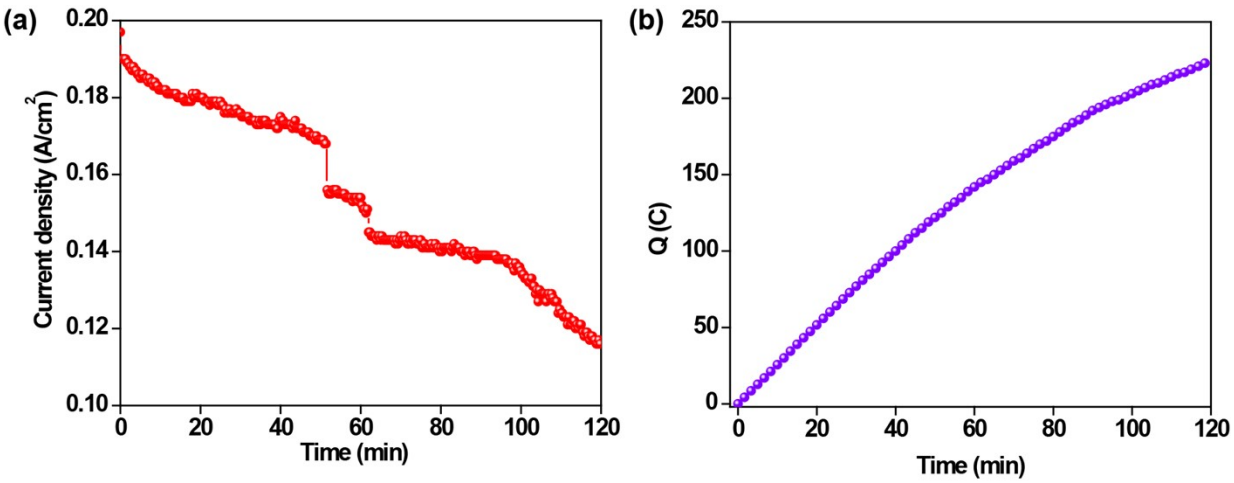

Fig. S14. (a) Chronoamperometric response observed and (b) number of charges involved in the HMF oxidation catalyzed by Rbf-Ni-MOF.

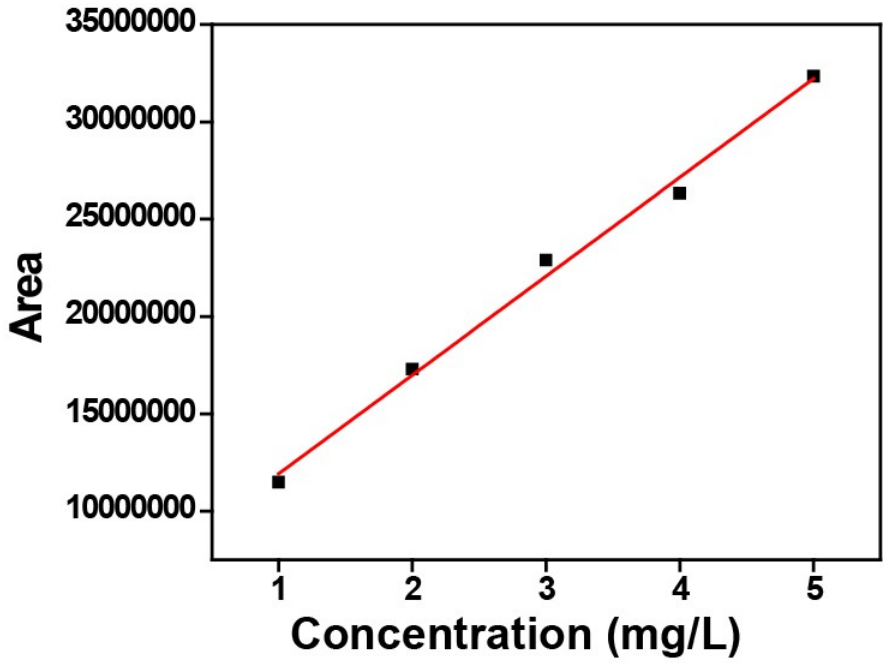

Fig. S15. Calibration curves for FDCA obtained from HPLC analyses.

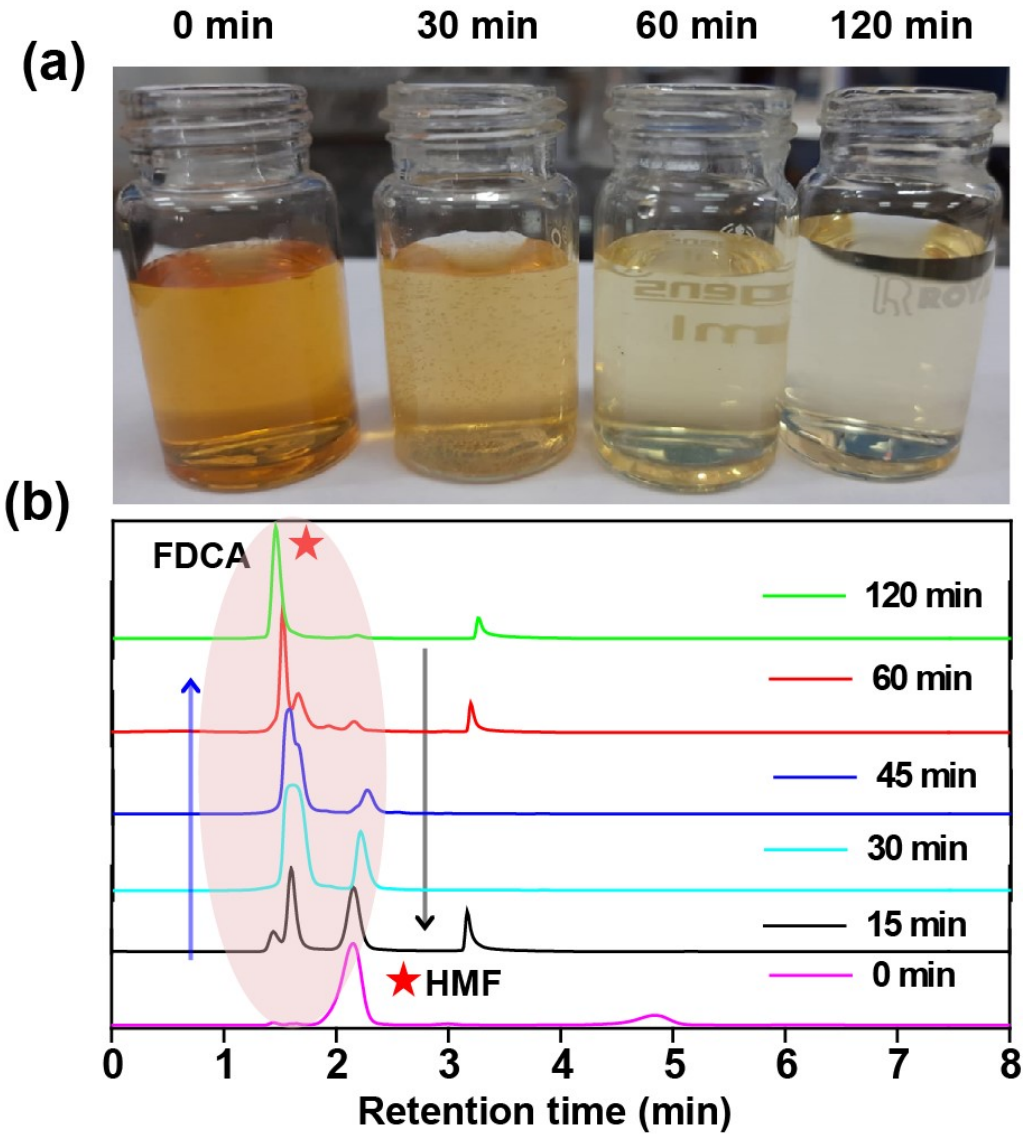

Fig. S16. (a) Photograph and (b) HPLC chromatograms of aliquots collected from anodic chamber at various time intervals.

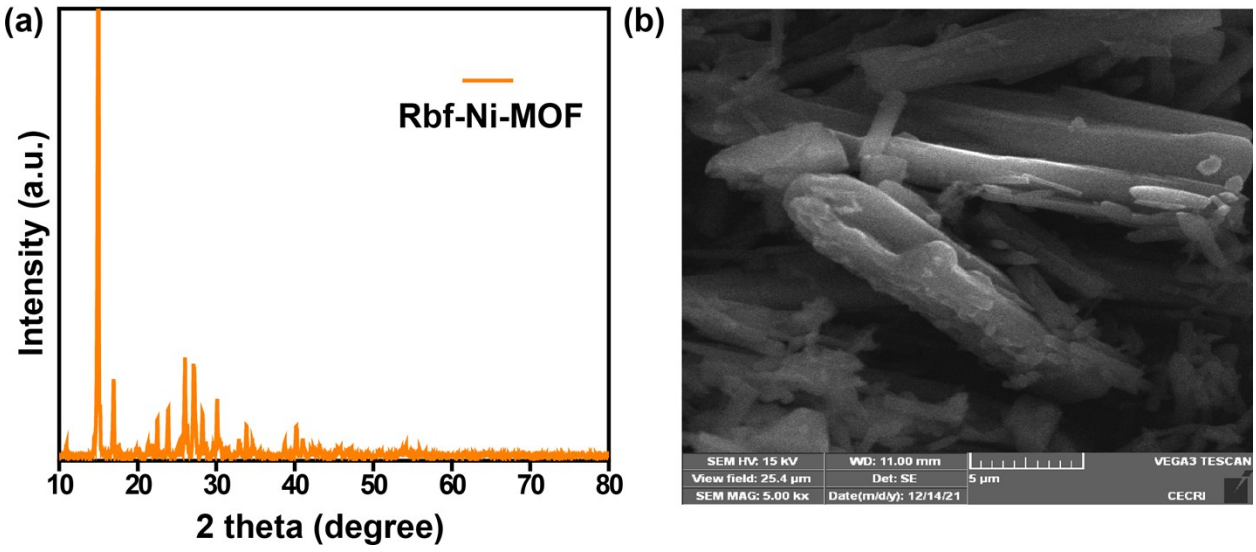

Fig. S17. (a) Powder X-ray diffraction pattern and (b) SEM image of the used Rbf-Ni-MOF in HMF oxidation.

Table S2. Comparison of the OER performance of the present material with the literature reports

Electrocatalyst	**Electrolyte**	**Overpotential**	**Tafel slope**	**Application (Ref.)**
[Fe–N–CCo_2(μ-OH)$_2$ (bbta)](MAF-X_{27}-OH)	1.0 M KOH	292 mV at 10 mA/cm^2	NA	OER (1)
MOF [{Fe_3(μ_3 -O)$(bdc)_3$}$_4${$Co_2(Na)_4(L^T)_2$}$_3$]	0.1 M KOH	283 mV at 10 mA/cm^2	43 mV /decade	OER (2)
NiCo-UMOFNs	1.0 M KOH	250 mV at 10 mA/cm^2	42 mV/decade	OER (3)
MIL-53(FeNi)/NF	1.0 M KOH	233 mV at 10 mA/cm^2	31.3 mV/decade	OER (4)
NiFe-MOF/NF	1.0 M KOH	195 mV at 10 mA/cm^2	48.5 mV /decade	OER (5)
$Ni_{0.83}Fe_{0.17}(OH)_2$ nanosheets	0.1 M KOH	245 mV at 10 mA/cm ^{2}	61 mV/decade	OER (6)
Ni(Fe)-MOF nanosheets	1.0 M KOH	227 mV at 10 mA/cm^2	38.9 mV/decade	OER (7)
NiFe LDH	1.0 M KOH	182 mV at 10 mA/cm^2	78.3 mV/decade	OER (8)
MIL-53(Co-Fe)/NF	1.0 M KOH	262 mV at 100 mA/cm ^{2}	69 mV/decade	OER (9)

$S_{0.05}$-Fe-BTB/NF	1.0 M KOH	231 mV at 20 mA/cm ^{2}	41 mV/decade	OER (10)
This work	**1 M KOH**	**220 mV at 10 mA/cm ^{2}**	**39 mV /decade**	**OER**

NA - Not available

Table S3. Comparison of the HMFOR performance of the present material with the literature reports.

Electrocatalyst	**Electrolyte**	**Applied potential**	**Fardaic efficiency**	**Application (Ref.)**
NiCoFe-LDHs nanosheets	1.0 M KOH	1.51 V *vs* RHE at 20 mA/cm^2	90 %	HMFOR (11)
CF-$Cu(OH)_2$	0.1 M KOH	0.8 V (*vs* Ag/AgCl) at 50 mA/cm^2	~100 %	HMFOR (12)
NiFe layered double hydroxide (LDH) nanosheets	1.0 M KOH	1.43 V *vs* RHE	99.4 %	HMFOR (13)
Electrodeposited Co−P	1.0 M KOH	1.38 V *vs* RHE at 20 mA/cm^2	~100 %	HMFOR (14)
Au-Pd catalyst	0.1 M KOH	0.90 V *vs* RHE	NA	HMFOR (15)
Cu_xS@NiCo-LDH	1 M KOH	1.32 mV at 10 mA/cm ^{2}	99 %	HMFOR (16)
NiS_x/Ni_2P nanotube arrays	1.0 M KOH	1.346 V *vs*. RHE	95.1 %	HMFOR (17)
Co_9S_8–Ni_3S_2@N,S,O-tri-doped carbon (NSOC) heterostructures	1.0 M KOH	1.55 V *vs* RHE	78.5 %	HMFOR (18)
This work	**1 M KOH**	0.8 V *vs* Ag/AgCl	95.0 %	**OER**

NA - Not available

References

1. X.-F. Lu, P.-Q. Liao, J.-W. Wang, J.-X. Wu, X.-W. Chen, C.-T. He, J.-P. Zhang, G.-R. Li and X.-M. Chen, *J. Am. Chem. Soc.*, 2016, **138**, 8336-8339.
2. J.-Q. Shen, P.-Q. Liao, D.-D. Zhou, C.-T. He, J.-X. Wu, W.-X. Zhang, J.-P. Zhang and X.-M. Chen, *J. Am. Chem. Soc.*, 2017, **139**, 1778-1781.
3. S. Zhao, Y. Wang, J. Dong, C.-T. He, H. Yin, P. An, K. Zhao, X. Zhang, C. Gao, L. Zhang, J. Lv, J. Wang, J. Zhang, A. M. Khattak, N. A. Khan, Z. Wei, J. Zhang, S. Liu, H. Zhao and Z. Tang, *Nat. Energy,* 2016, **1**, 16184.
4. F. Sun, G. Wang, Y. Ding, C. Wang, B. Yuan and Y. Lin, *Adv. Energy Mater.*, 2018, **8**, 1800584.
5. J. Liang, X. Gao, B. Guo, Y. Ding, J. Yan, Z. Guo, E. C. M. Tse and J. Liu, *Angew. Chem. Int. Ed.,* 2021, **60**, 12770-12774.
6. Q. Zhou, Y. Chen, G. Zhao, Y. Lin, Z. Yu, X. Xu, X. Wang, H. K. Liu, W. Sun and S. X. Dou, *ACS Catal.,* 2018, **8**, 5382-5390.
7. C. Cao, D.-D. Ma, Q. Xu, X.-T. Wu and Q.-L. Zhu, *Adv. Funct. Mater.,* 2019, **29**, 1807418.
8. Z. Qiu, C.-W. Tai, G. A. Niklasson and T. Edvinsson, *Energy Environ. Sci.,* 2019, **12**, 572-581.
9. M. Xie, Y. Ma, D. Lin, C. Xu, F. Xie and W. Zeng, *Nanoscale*, 2020, **12**, 67-71.
10. C. Ling, X. Leng, X.-J. Lu, J.-H. Li, Z. Yang and A.-W. Xu, *J. Mater. Chem. A,* 2022, **10**, 17246-17253.
11. M. Zhang, Y. Liu, B. Liu, Z. Chen, H. Xu and K. Yan, *ACS Catal.,* 2020, **10**, 5179-5189.
12. X. Pang, H. Bai, H. Zhao, W. Fan and W. Shi, *ACS Catal.,* 2022, **12**, 1545-1557.
13. W.-J. Liu, L. Dang, Z. Xu, H.-Q. Yu, S. Jin and G. W. Huber, *ACS Catal.,* 2018, **8**, 5533-5541.
14. N. Jiang, B. You, R. Boonstra, I. M. Terrero Rodriguez and Y. Sun, *ACS Energy Lett.*, 2016, **1**, 386-390.
15. D. J. Chadderdon, L. Xin, J. Qi, Y. Qiu, P. Krishna, K. L. More and W. Li, *Green Chem.,* 2014, **16**, 3778-3786.
16. X. Deng, X. Kang, M. Li, K. Xiang, C. Wang, Z. Guo, J. Zhang, X.-Z. Fu and J.-L. Luo, *J. Mater. Chem. A,* 2020, **8**, 1138-1146.
17. B. Zhang, H. Fu and T. Mu, *Green Chem.,* 2022, **24**, 877-884.

18. M. Cai, Y. Zhang, Y. Zhao, Q. Liu, Y. Li and G. Li, *J. Mater. Chem. A,* 2020, **8**, 20386-20392.